ESD-TR-88-326

Technical Report
844

Design Considerations and Experimental Results for Direct-Detection Spatial Tracking Systems

E.A. Swanson
J.K. Roberge

4 April 1989

Lincoln Laboratory
MASSACHUSETTS INSTITUTE OF TECHNOLOGY
LEXINGTON, MASSACHUSETTS

**Prepared for the Department of the Air Force
under Electronic Systems Division Contract F19628-85-C-0002.**

The work reported in this document was performed at Lincoln Laboratory, a center for research operated by Massachusetts Institute of Technology, with the support of the Department of the Air Force under Contract F19628-85-C-0002.

This technical report has been reviewed and is approved for publication.

FOR THE COMMANDER

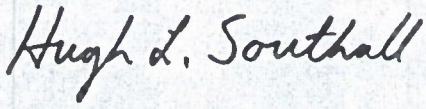

Hugh L. Southall, Lt. Col., USAF
Chief, ESD Lincoln Laboratory Project Office

MASSACHUSETTS INSTITUTE OF TECHNOLOGY
LINCOLN LABORATORY

DESIGN CONSIDERATIONS AND EXPERIMENTAL RESULTS FOR DIRECT-DETECTION SPATIAL TRACKING SYSTEMS

E.A. SWANSON
Group 67

J.K. ROBERGE
Group 63

TECHNICAL REPORT 844

4 APRIL 1989

LEXINGTON MASSACHUSETTS

ABSTRACT

The effect of signal and background shot noise, as well as device noise, on the performance of a direct-detection spatial tracking system is investigated for arbitrary detector arrays assuming linear loop operation. The performance of quadrant detectors as a function of background radiation and detector radius is then analyzed and compared with some performance bounds. APD- and PIN-based tracking systems also are compared. The effects of non-focal-plane processing, focus error, and pupil walk on tracking performance are investigated. Experimental results of a 2.4-kHz two-axis tracking loop operating at low signal power using an APD quadrant detector are presented.

TABLE OF CONTENTS

LIST OF ILLUSTRATIONS

LIST OF TABLES

DESIGN CONSIDERATIONS AND EXPERIMENTAL RESULTS FOR DIRECT-DETECTION SPATIAL TRACKING SYSTEMS

1. INTRODUCTION

The spatial tracking system for optical radar and communication is of critical importance because optical antennas have such narrow beamwidths (~μrad). Even a very good optical platform may have angular disturbances on the order of a few milliradians, and optical systems typically require angular stabilization to a fraction of a beamwidth. Thus, a spatial tracking system with high precision, large bandwidth, and large dynamic range is necessary. A number of papers have been written on the design of such tracking systems.[1-8] Here, we discuss some additional design considerations and present some experimental results.

A simplified block diagram of a typical spatial tracking system is shown in Figure 1. The tracking system control signal is generated from the tracking detector array, which is typically located in a focal plane. If the angle of incidence of the received optical field is accurately tracked, the focal spot will remain centered. If the spot is not centered, error signals are generated and fed back to a fast steering mirror (FSM) to correct for the errors. Typically, to achieve high bandwidths the FSM has a small angular range. Therefore, to keep the FSM within its operation range, the low-frequency large-amplitude disturbances are nulled with a large coarse pointing mirror (CPM) or a gimballed telescope. This nested servo design can provide a dynamic range of more than 10^6:1, low-frequency disturbance rejection in excess of 140 dB, and –3-dB closed-loop bandwidths in excess of 2.4 kHz.

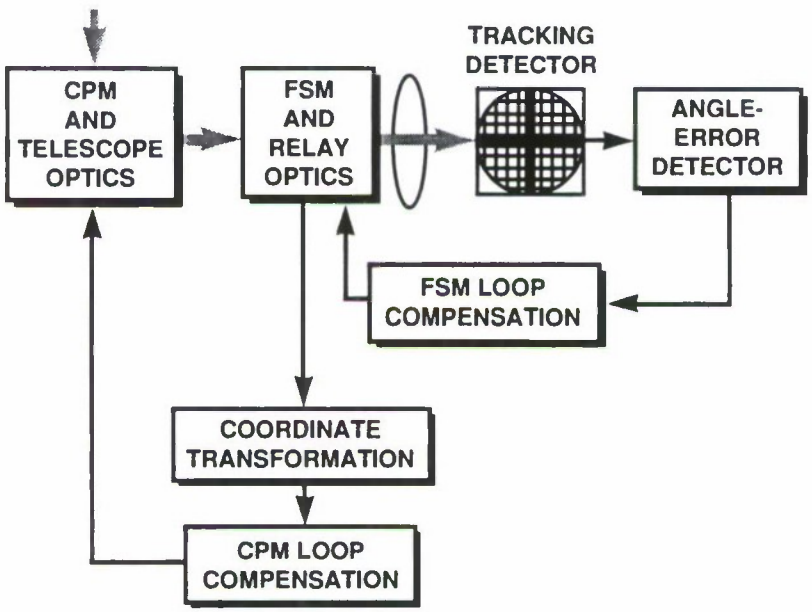

116455-1

Figure 1. Tracking system structure.

In this report, we focus on the high-bandwidth tracking loop. We develop bounds and estimates of noise performance; compare the performance of two commonly used detectors, avalanche photodetectors (APDs) and PIN detectors; discuss the effects of wavefront error and non-focal-plane processing; and, in the section on experimental results, discuss a tracking-error-normalization and loop-compensation technique and present quantitative data on loop rejection and noise performance.

In optical radar and communication systems the boresight, acquisition, and pointing subsystems are closely integrated with the spatial tracking subsystem. However, these subsystems will not be discussed. It is assumed that acquisition has been accomplished and that the incident optical field has a flat phase front.

2. NOISE PERFORMANCE

2.1. General Noise Performance Bounds

As long as the tracking loop operates in its linear region, it can be represented by the standard model of Figure 2. K_d represents the angle discriminator gain. In this simplified model, the total tracking error is given by

$$\sigma_T^2 = \sigma_{uc}^2 + NEA^2 \tag{1}$$

where σ_{uc} is the uncompensated tracking error, and NEA (noise-equivalent angle) is noise-induced tracking error. Rewriting this expression in terms of the power spectrum of the angular disturbance $S_\theta(f)$, the closed-loop transfer function of the tracking loop H(f), and the noise-equivalent spectral density (NESD), yields the well-known expression

$$\sigma_T^2 = \int_{-\infty}^{\infty} |1 - H(f)|^2 S_\theta(f)\, df + \frac{NESD}{2} \int_{-\infty}^{\infty} |H(f)|^2\, df \quad . \tag{2}$$

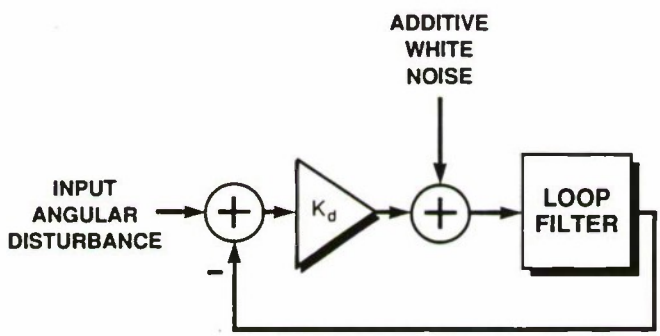

116455-2

Figure 2. Simplified one-dimensional linear loop model.

The NESD is equal to the (single-sided) spectral height of the additive white noise divided by the square of the angle discriminator gain. The additive noise has been assumed to be spectrally white. Most of the noise sources such as signal, background, and dark current shot noise as well as thermal noise are well modeled as white noise.[9] There are circuit and detector noise sources that give rise to non-white noise,[10] but, as we will see in Section 4, over a small bandwidth the approximation of a white-noise source yields good experimental results. Rewriting Equation (2) in terms of the loop rejection R(f) and noise equivalent bandwidth (NEB)

$$\sigma_T^2 = \int_{-\infty}^{\infty} |R(f)|^2 S_\theta(f)\, df + NESD\, NEB \quad . \tag{3}$$

Therefore, NEA for each angular axis is equal to the square root of the product of the NESD and the NEB. The noise bandwidth of the tracking loop as well as the uncompensated tracking error are governed by the dynamics of the loop and angular disturbance. In this section, we develop bounds on noise-induced tracking error. To make these bounds independent of loop dynamics and valid for arbitrary angular disturbances, we focus on minimizing the NESD for an arbitrary number of detectors placed symmetrically about the x and y axes. In Section 4, we will discuss tracking loop rejection and loop dynamics.

To minimize the overall tracking error, it is necessary to minimize the NESD. The loop dynamics can be optimized separately once the angular disturbance is modeled. It can be shown that, for a linear tracking loop, minimizing the NESD is necessary to achieve a minimum mean-square error. Furthermore, as the number of photons per coherence time of the angular process becomes large, the Poisson statistics governing the observation equation approach Gaussian. Minimizing the NESD is then necessary to achieve many other performance bounds such as the Cramér-Rao bound.[11] It should be noted that for certain loop designs the uncompensated tracking error may dominate the NEA. Under such circumstances, optimizing the NESD will not dramatically reduce the overall tracking error but will add additional margin to the tracking system signal power link budget.

Assuming that the loop is operating in its linear region, the currents out of each detector element can be linearized about the azimuth and elevation tracking errors. Expressions for the noise out of each detector based on signal shot noise, background shot noise, dark current, front-end amplifier noise, and excess noise factor (in the case of detectors with gain) can be derived.[12] Optimally combining all the detector outputs yields the minimum NESD, which is given by[11]

$$NESD = \left[\sum_{ij=1}^{\infty} \frac{P_m \left[S_{ij} \frac{\eta P_s}{h\nu} \right]^2}{2 \left[F(G_{ij}) \left(S_{ij} \frac{\eta P_s}{h\nu} + \frac{\eta P_{bij}}{h\nu} + 4\frac{I_{dbij}}{e} \right) + 4 \left(\frac{\frac{I_{dsij}}{e} + \frac{N_{ocij}}{2e^2}}{G_{ij}^2} \right) \right]} \right]^{-1} \tag{4}$$

where

$$\dot{S}_{ij} = 4 \int_{\Omega ij} \frac{\partial I_s(x,y)}{\partial x} dxdy \tag{5}$$

$$S_{ij} = 4 \int_{\Omega ij} I_s(x,y)\, dxdy \tag{6}$$

$$P_{bij} = 4 \int_{\Omega ij} I_b(x,y)\, dxdy \tag{7}$$

P_m = normalized intensity modulation power

P_s = optical signal power

η = detector quantum efficiency

ν = optical frequency

h = Planck's constant

$I_s(x,y)$ = normalized signal intensity distribution

$I_b(x,y)$ = background intensity distribution

x and y represent spatial coordinates at the detector

Ω = integration area across a detector element

F(G) = excess noise factor

I_{db} = gain dependent dark current

I_{ds} = gain independent dark current

e = electron charge

N_{oc} = total single-sided front-end current noise spectral density

G = detector gain.

The infinite summation is over one quadrant, and the subscripts "ij" identify parameters associated with each detector element.

In many tracking systems, the use of intensity modulation is warranted because it eliminates sensitivity to 1/f and dc disturbances from the detectors, amplifiers, and background sources. Since the modulation depth cannot be >1, P_m must be ≤1. Assuming coherent demodulation and a modulation depth of m, $P_m = m^2$ for square-wave modulation, $= (4/\pi)^2\, m^2/2$ for square-wave modulation using only the

fundamental harmonic in demodulation, and = $m^2/2$ for sinusoidal intensity modulation. For ideal CW operation, $P_m = 1$.

In addition to increased modulation power, square-wave modulation in some cases offers an additional performance improvement in the presence of background radiation. Such cases arise when the optical frequency is modulated by the same parameter that is varied to modulate the intensity (i.e., semiconductor lasers). With square-wave modulation, an interference filter need only be wide enough to encompass the optical frequency uncertainty when the source is in its high-power state (~Å); whereas, with sinusoidal modulation, the interference-filter bandwidth must be wider than the frequency uncertainty plus the modulation bandwidth (~10 Å). A narrower interference filter leads to reduced background noise.

Equation (4) can be optimized for a wide variety of parameters. To compare our results with those of others, we analyze Equation (4) for three different cases.

2.2. Signal or Background Shot-Noise-Limited Operation

It is assumed that the detector dark currents and front-end amplifier noise are equal to zero (G = 1, F = 1). Under these assumptions, there is no loss in assuming that each detector element is infinitesimal since they can always be grouped to form a larger detector with no additional noise. In the limit as each Ω_{ij} approaches zero, Equation (4) becomes

$$\mathrm{NESD} = \left[2 P_m \frac{\eta P_s}{h\nu} \int_0^\infty \int_0^\infty \frac{\left[\frac{\partial I_s(x,y)}{\partial x} \right]^2}{I_s(x,y) + \frac{I_b(x,y)}{P_s}} \, dx \, dy \right]^{-1} . \tag{8}$$

Rewriting Equation (8) in terms of the amplitude of the signal field and assuming that there is no background radiation yields a lower bound for the NESD, which is given by

$$\mathrm{NESD} \geq \left[8 P_m \frac{\eta P_s}{h\nu} \int_0^\infty \int_0^\infty \left[\frac{\partial U_s(x,y)}{\partial x} \right]^2 dx \, dy \right]^{-1} . \tag{9}$$

This expression is identical to the corresponding bound for heterodyne detection except for a factor of $2P_m$ (see Reference 5). That is, for ideal CW operation, direct detection is superior by 3 dB. (This analysis is based on the first and second moments of the observation. As pointed out in Section 2.1, the direct-detection and heterodyne-detection have similar statistics only when the number of detected photons per loop time-constant becomes large.)

The bounds for Airy-disk and Gaussian focal-plane intensity distributions are given by

$$\mathrm{NESD} \geq \left[P_m \frac{\eta P_s}{h\nu} \frac{\pi^2}{2} \frac{1}{\left(\frac{\lambda}{d}\right)^2} \right]^{-1} \text{ Airy disk} \tag{10}$$

$$NESD \geq [\, P_m \frac{\eta P_s}{h\nu} \frac{1}{\sigma^2} \,]^{-1} \quad \text{Gaussian} \tag{11}$$

where λ is the optical wavelength, d is the aperture diameter, and σ is the radius at which the intensity is reduced by 1/e point. (Note that σ is related to ω_s, the radius at which the amplitude is down by 1/e in the pupil-plane, by $\sigma = (1/\sqrt{2\pi})\,(\lambda/\omega_s)$.

2.3. Signal or Detector Shot-Noise-Limited Operation (Gaussian Field)

It is assumed that there is a Gaussian intensity distribution, no background radiation, unity gain detectors (G = 1, F = 1), and square detector elements with equal area and distance **a** on each side. The objective is to find the NESD as a function of **a**. The result is given in Figure 3, where $\lambda_s = P_s/h\nu$ and $\lambda_n = [(I_d/e) + N_{oc}/2e^2]$. It is clear that there is no merit in using detector arrays larger than a quadrant detector except when the device noise is near zero. This reflects the fact that spreading the signal field over many detectors to increase resolution does not offset the increase in noise from the added detectors. Even when there is no detector noise, the improvement of an infinite detector array over a quadrant detector is <2 dB. As we will see in Section 2.4, for an Airy-disk intensity distribution an infinite detector array can improve performance over a quadrant detector array by ~4.8 dB. Still, in many applications the increased performance afforded by higher order detector arrays is not worth the added complexity.

As seen in Figure 3, once the quantity $\mathbf{a}/\sigma$ is greater than ~2, the tracking performance remains relatively constant and close to optimal. It is of interest to compare the tracking results with those from estimating the centroid of the intensity profile.[13] Under similar assumptions, the optimal $\mathbf{a}/\sigma$ ratio for centroiding was found to be between 2.1 and 3.5. The upper limit results from the spot size becoming very small; it can be lost within one detector element unless it is near the edge. This is not a problem

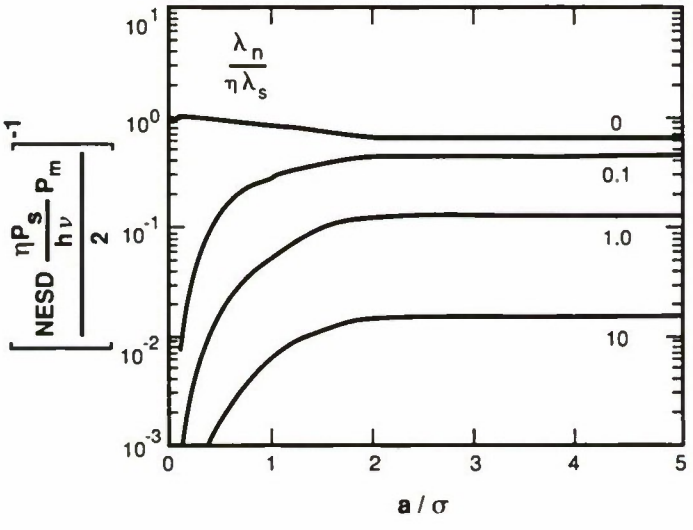

Figure 3. NESD as a function of ratio of detector to spot size.

in the tracking scenario, since the spot is being stabilized at the intersection of four detectors. In situations where both acquisition and tracking are to be performed with the same detector array, if the quantity a/σ remains within the intersection of the optimal tracking range and the optimal acquisition range, which is a/σ between 2.1 to 3.5, near-optimal tracking and acquisition performance can be achieved simultaneously.

2.4. Signal or Background Shot-Noise-Limited Operation with a Quadrant Detector

Section 2.3 showed that, for a Gaussian intensity distribution, a quadrant detector was essentially optimum. We will now find the optimum radius for a circular quadrant detector. For a quadrant detector, P_b can be expressed as shown in Equation (12), where r is the radius of the detector and λ/d represents the diffraction-limited beamwidth. We assume that the background radiation is from an extended source with a spectral radiance of $N(\lambda)$ and that the optical bandwidth is W:

$$P_b = 4\, P_{bo} \left[\frac{r}{(\frac{\lambda}{d})} \right]^2 \tag{12}$$

$$P_{bo} = (\frac{\pi}{4})^2\, N(\lambda)\, \lambda^2\, W \tag{13}$$

Assuming an Airy-disk intensity distribution and the detector dark current and front-end amplifier noise equal to zero (F = 1), the NESD as a function of detector radius can be found (Figure 4). For the case of no background radiation, the optimum detector radius is about 1.22 λ/d (the first null of the Airy disk) and the performance is 4.8 dB below the optimal performance given by Equation (10). As the background radiation increases, the optimum radius slowly decreases. In practice, larger FOV detectors with their associated larger pull-in range are often used to minimize the requirements of the spatial acquisition system.

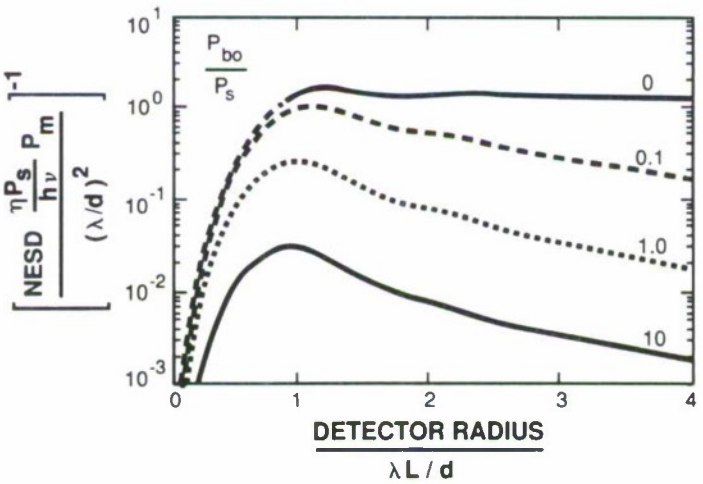

116455-4

Figure 4. NESD vs quadrant detector radius.

2.5. Comparison of APD- and PIN-Based Tracking Systems

We now compare the performance of APD- and PIN-based tracking systems. For the APD-based tracking system, the gain can be optimized to minimize the NESD. For some APDs, the dependence of excess-noise factor on gain is given by[9,10]

$$F = \left(2 - \frac{1}{G} \right) (1 - k) + k G \tag{14}$$

where k is the effective ionization rate ratio. Assuming small k and large G, the optimum APD gain is given by

$$G_o = \left[\frac{8 \left(\frac{I_{ds}}{e} + \frac{N_{oc}}{2e^2} \right)}{k \left(S \frac{\eta P_s}{h\nu} + \frac{\eta P_b}{h\nu} + 4 \frac{I_{db}}{e} \right)} \right]^{1/3} . \tag{15}$$

Figure 5 contains the comparison of each tracking system to an "ideal" detector which is assumed to have the unity quantum efficiency, no dark-current noise, and no front-end circuit noise. The parameters assumed in the comparison are given in Table I. Three different background sources are investigated: no background, strong earth background, and solar background. An Airy-disk focal-plane intensity distribution and a quadrant detector with a radius of 2.5 beamwidths are assumed. The APD and front-end noises are values that have been measured in our laboratory.[10] The comparison is made in terms of the ratio of the power required of each tracking system to the "ideal" detector tracking system in

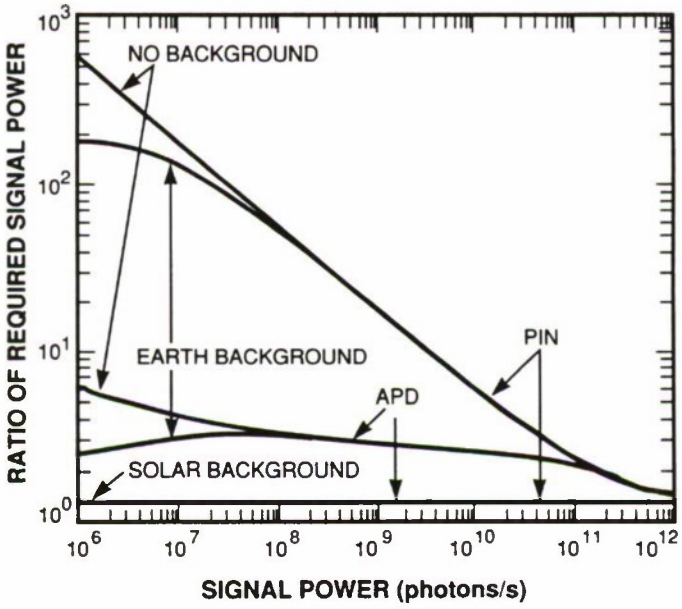

116455-5

Figure 5. APD and PIN vs ideal detector performance.

TABLE I

APD and PIN Performance Parameters

λ	0.8 μm
Detector Radius	2.5 λ/d
$S_{11} = 0.92$	
$S_{11} = 1.64/(\lambda/d)$	
N_{oc}	2.0×10^{-27} A^2/Hz
P_b	1.83 pW [$N(\lambda) = 0.024$ W/(m^2Å sr)] earth[14,15]*
	140 nW [$N(\lambda) = 1800$ W/(m^2Å sr)] sun[14,15]*
W	25 Å

APD Parameters	PIN Parameters
$\eta = 0.8$	$\eta = 0.8$
$I_{db} = 0.01$ pA	$I_{db} = 0$
$I_{ds} = 1.0$ nA	$I_{ds} = 1.0$ nA
$k = 0.01$	$k = 0$
Gain = 1 to 200	Gain = 1

* Background assumes 3-dB loss due to a polarizer, and 2-dB loss due to optical attenuation.

order to achieve the same NESD. As expected, for background-limited operation (such as the solar background) or for signal shot-noise-limited operation (>10^{12} photons/s), the APD and PIN systems perform identically. However, for low backgrounds the APD-based system can offer over 20 dB of improved performance. The plateaus at low signal powers are the regions in which the PIN- and APD-based systems are background shot-noise-limited. Note that the APD performs within 3 to 5 dB of the ideal detector unless it becomes gain-dependent dark-current-limited; 3 dB of this loss can be attributed directly to the APD excess-noise factor [Equation (14)]. The fact that the additional loss is small is a result of the relatively low gain-dependent dark current and the low ionization rate ratio.

3. NON-FOCAL-PLANE PROCESSING

We now investigate the effect of non-focal-plane processing, focus error, and pupil walk on tracking performance, assuming that the incident optical field is Gaussian and that an infinite area quadrant detector is used. Using the Fresnel diffraction equation to find the field distribution at an arbitrary distance from a focusing lens, the sum-channel and angle-discriminator profiles can be found and are given by

$$\Sigma = P_s \tag{16}$$

$$\Delta_x = P_s \, \mathrm{erf}\left[\frac{\theta_x + \left(\frac{1}{L} - \frac{1}{f}\right) O_x}{\left(\frac{\lambda}{2\pi\sigma}\right) X} \right] \tag{17}$$

where

$$X = \left[1 + \left[\frac{\left(\frac{\sigma}{L}\right)\left(1 - \frac{L}{L_o}\right)}{\left(\frac{\lambda}{2\pi\sigma}\right)} \right]^2 \right]^{1/2} \tag{18}$$

$$\frac{1}{L_o} = \frac{1}{f} - \frac{1}{R_o} \tag{19}$$

Σ = sum-channel profile,

Δ_x = x-axis difference-channel profile,

erf (.) = error function,

θ_x = x-axis angle of incidence of the optical field at the focusing lens,

L = distance from the focusing lens to the detector array,

f = focal length,

O_x = x-axis lateral offset of the optical beam at the focusing lens,

R_o = radius of curvature of the field incident onto the focusing lens.

We now investigate the sensitivity of the NESD to the placement of the tracking detector array. By assuming small tracking errors so that the error function can be linearized, minimizing the NESD is equivalent to maximizing the slope of the angle discriminator or equivalently minimizing X. Optimum performance is obtained when the detector array is placed at L_o. This distance is equal to the focal length only when the incident optical field is perfectly collimated ($R_o = \infty$). If $L = L_o + \epsilon$, then

$$\epsilon \approx \left(\frac{\lambda L_o}{2\pi\sigma}\right)\left(\frac{L_o}{\sigma}\right)\left(X^2 - 1\right)^{1/2} \tag{20}$$

The first term on the right-hand side can be interpreted as the diffraction-limited spot size, the second term as the f-number of the focusing lens, and the third term as a loss factor. For example, if only a 1.5-dB loss in tracking performance ($X = \sqrt{2}$) is acceptable and an f# = 1 beam is used, the tracking-detector array must be placed to within one diffraction-limited spot size of the true location of the focal plane. This restriction can place stringent thermal and mechanical tolerances on the optical system

design. For large f-numbers, the linearization used to obtain Equation (20) may be invalid and Equations (18) and (19) must be used directly.

We now investigate the sensitivity of the NESD to focus error, assuming the tracking detector is placed in the optimal location for an unaberrated system (L = f). If focus errors are introduced from somewhere within the optical system, then the tracking performance will be degraded as a result of thermal or mechanical distortion or a design residual. If N is the number of waves of defocus, then

$$N = \frac{\sigma^2}{2\lambda R_o} = \frac{(X^2 - 1)^{1/2}}{4\pi} \quad . \tag{21}$$

Again, if the loss in tracking performance is to be <1.5 dB, the focus error must be kept to $<\lambda/13$.

We now investigate the effect of the lateral offset from the optic axis. As seen from Equation (17), if the detector array is not placed at the focal distance the offset appears as a bias term in the error signal. If the bias becomes significant compared with $\lambda/(2\pi\sigma)$ X, then the angle discriminator will become nonsymmetrical and its effective slope will be reduced. The dynamic range over which the angle discrimination remains linear can be chosen by adjusting the location of the detector L. For example, if a 1-dB compression in the discriminator linearity is acceptable at a maximum angle θ_{max}, then the detector array should be placed at

$$L = \{\frac{1}{L_o} \pm \frac{1}{\sigma}[(\frac{\theta_{max}}{0.875})^2 - (\frac{\lambda}{2\pi\sigma})^2]^{1/2}\}^{-1} \quad . \tag{22}$$

However, this increased dynamic range is not only at the expense of noise performance. It can lead to a limited angular rejection capability. If the pupils within the optical system are not tightly controlled or if the FSM does not have its center of rotation about the front surface of the mirror, the offset at the focusing lens will be a function of the angular disturbance. For example, if the angular disturbance has an incidence angle θ_i with respect to the FSM normal when it is at null and the mirror normal is displaced by an angle θ_m from null, then if the center of rotation of the FSM is a distance D behind the front surface of the mirror it can be shown that

$$O = 2\,D \sin(\theta_i + \theta_m)[1 - \cos(\theta_m)] \quad . \tag{23}$$

If the θ_o is the nominal angle of incidence and the mirror operates around its null, then

$$O \approx 2\,D \sin(\theta_o)\,\theta_m \quad . \tag{24}$$

Since θ_m represents one-half the estimated incidence angle, it is straightforward to show that, unless the standard tracking algorithm is modified, the maximum rejection R_{max} is given approximately by

$$R_{max} = D \sin(\theta_o)(\frac{1}{L} - \frac{1}{f}) \quad . \tag{25}$$

If D = 20 mm, $\theta_o = 45°$, f = 20 cm, and L is positioned to within 1 percent, then R_{max} is only 63 dB.

4. EXPERIMENTAL RESULTS

The goal of our experimental work was to demonstrate two-axis high-precision tracking using relatively large bandwidth and low signal power. A block diagram of our experimental configuration is depicted in Figure 6. The light source was a GaAlAs laser diode operating at 0.83μm. Its optical output was sinusoidally intensity modulated at 54 kHz with a modulation depth that could be varied from 0 to 100 percent. An anamorphic pair was used to convert the light beam from elliptical to circular. A 20:1 beam expander and an aperture stop were used to transform the Gaussian intensity distribution to a 5-mm-diam. collimated beam of uniform intensity. This beam was directed onto a beam-steering mirror that was used to introduce two-dimensional angular disturbances into the tracking loop. Simulated platform disturbances as well as sinusoidal disturbances could be injected to analyze loop performance. The beam-steerer had internal angular monitoring so that the disturbance injected into the loop could be accurately determined.

A 1:1 relay was used to relay the pupil from the randomizing beam-steerer onto the FSM. If the loop was operating correctly, the FSM would correct for the disturbance introduced by the randomizing beam-steerer. The light was then split into three different paths. One path led to a television monitor. The focusing lens and imaging optics were configured so that the Airy-disk pattern could be viewed.

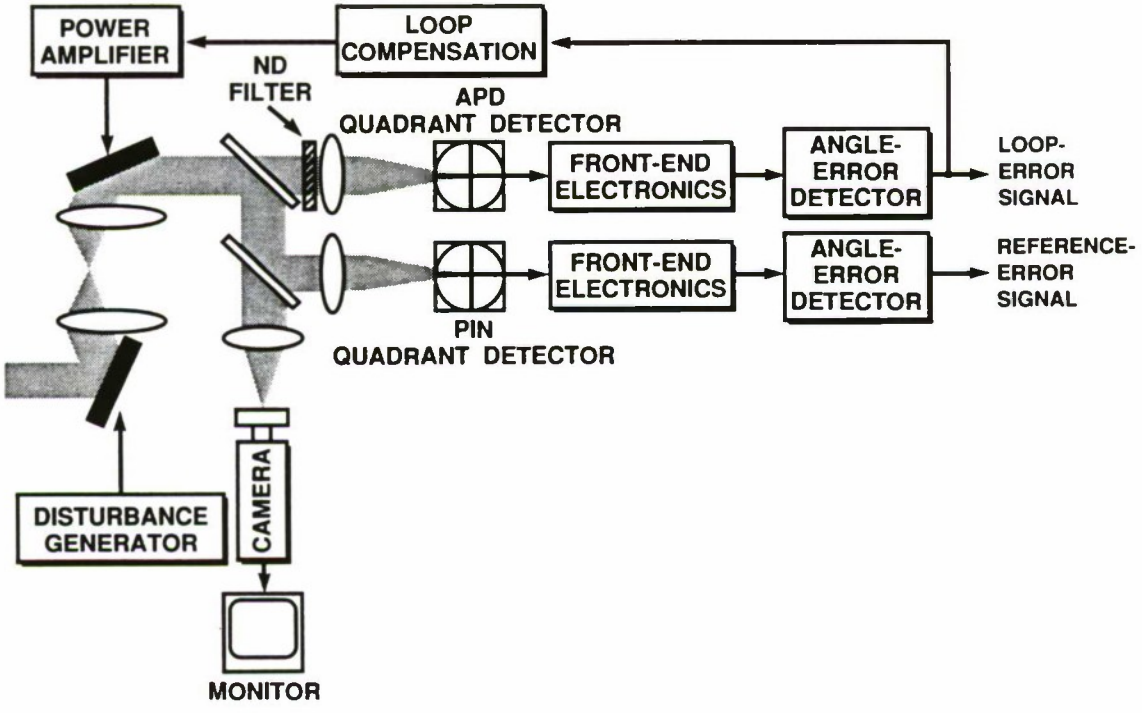

Figure 6. Experimental setup.

This configuration allowed for easy alignment and a coarse check of tracking performance. The middle path served as a reference path to monitor tracking performance. The reference error signal was formed by using a commercially available PIN quadrant detector, four transimpedance amplifiers (TIAs), and a summing network. The summing network derived the baseband azimuth and elevation error signals by simple addition, subtraction, and low-pass filtering to remove the IF components.

The top path formed part of the tracking loop. A neutral density filter served to set the nominal received signal power. To achieve low-noise performance, a quadrant APD was needed. Unfortunately, there are no commercially available quadrant APDs that meet our requirements of low noise, narrow dead zone, and gain uniformity. Therefore, we created one by using four discrete APDs, some imaging lenses, and a four-way reflecting pyramid splitter. A 302-mm focusing lens was used to focus a spot onto the tip of the image splitter. The focal length was chosen to form a spot size that was more than ten times the dead zone of the image splitter. Four lenses placed one focal length away from the tip of the pyramid were used to collect the reflected light beams and image a pupil onto each of the detectors located one focal length away. Imaging a pupil onto each of the four detectors minimized the motion of the spot across the detector surface, and therefore minimized the effect of gain uniformities across the face of the APD.

Each of the four APDs had a slightly different gain dependence on bias voltage. This variation, combined with the open-loop accuracy of the bias voltage supplies, led to the need for a gain-balancing algorithm. Each APD would be biased according to the desired gain and gain-vs-bias-voltage curve for APD 1. The light hitting APD 1 was maximized by monitoring the voltage at 54 kHz from TIA 1 using a hill-climbing procedure. Next, the light out of APD 2 was maximized. The bias-voltage supply for APD 2 was then servoed until the voltage out of TIA 2 was equal to TIA 1. The remaining APDs were biased in the same fashion. This procedure was automated on a computer controller. Successful results were obtained. In fact, if the bias voltages corresponding to two gain settings were recorded before tracking was initiated, it was found that the gains could be switched during tracking without losing lock. This procedure also canceled the effects of gain differences in some of the front-end electronics.

The outputs of the APDs were fed directly into low-noise TIAs. A 10-MΩ feedback resistor was used in each TIA. This value represented a good compromise between minimizing thermal noise, the effect of amplifier voltage noise, and allowing a front-end bandwidth in excess of 100 kHz. At 54 kHz, the total effective front-end noise was only 1 dB above the thermal noise of the feedback resistor. The TIA outputs were high-pass filtered to remove low-frequency noise, amplified, and sent into a summing network to derive azimuth, elevation, and sum signals. The three signals were bandpass filtered and then sent into a normalizing network. The bandwidth of the sum-channel filter could be made relatively narrow since it does not affect loop dynamics (except during changes in signal power). The bandwidths of the difference channels must be wide relative to the desired loop bandwidth so that the loop phase margin is not compromised, but narrow enough so that the noise at the harmonics of the carrier is eliminated before mixing down to baseband.

To achieve constant loop bandwidth over a wide range of received signal power, it was necessary to normalize the signals proportional to the angular errors by the power in the sum channel. The sum channel was split into two paths. The first path was sent to a magnitude detector, the output of which

was used in a translinear circuit to normalize the difference signal. The second path was sent to a hard limiter that was used to create a reference to demodulate the normalized difference channels. Normalizing at IF and then mixing down to baseband as opposed to demodulating and then normalizing has the advantage of minimizing the effect of dc offsets since the system can be ac coupled right up to the demodulator. Identical designs are used for the azimuth and elevation loops. (In addition to this normalization technique, another based on converting the angular error into a relative phase shift between a pair of IF signals and then using double-balanced phase detectors to extract the normalized angle error was investigated.[16] The two methods yielded similar results.)

The normalized error signal is sent into the loop compensation network. The compensator was designed to achieve a type-two loop with a crossover frequency of 1 kHz and to provide 6 dB of gain margin and 45° of phase margin at the crossover frequency. The open-loop transfer function from the input to the power amplifier to the output of the angle error detector is indicated in Figure 7. This transfer function was measured by driving the input to the FSM power amplifier and measuring the output of the loop-angle error detector. Note that the FSM behaves as a lightly damped second-order circuit with a natural frequency of about 112 Hz. This frequency is equal to the square root of the flexure spring constant divided by the moment of inertia of the rotor and mirror. A secondary resonance is evident at about 9 kHz. It is this resonance that limits the ultimate closed-loop bandwidth obtainable with the FSM.

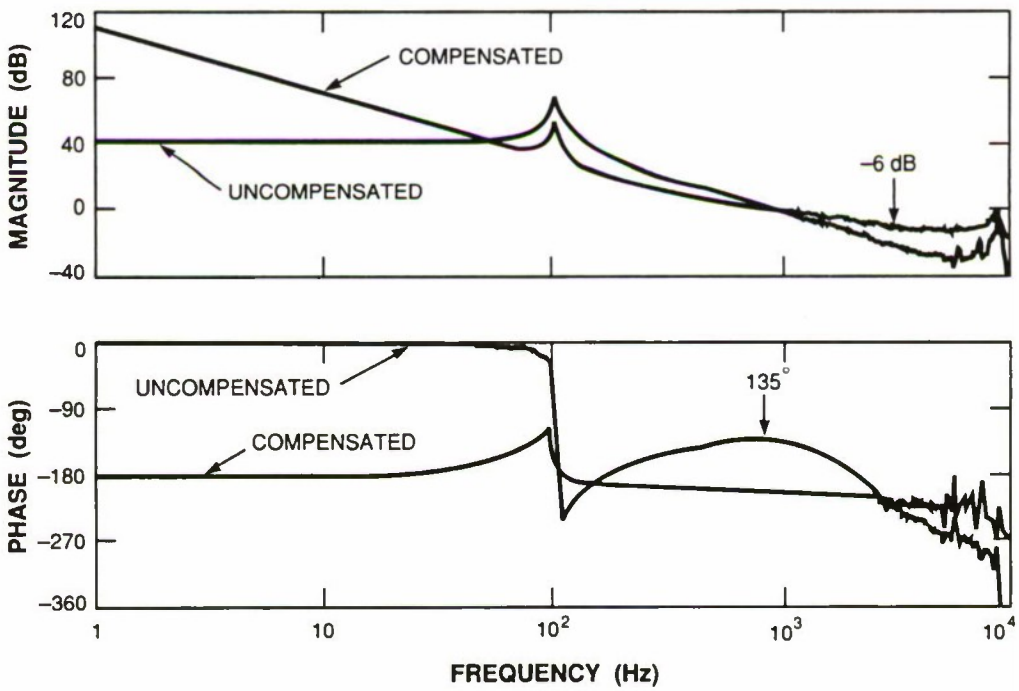

Figure 7. Measured open-loop transfer functions.

The departure from 180° of the uncompensated transfer function is mainly a result of losses in the magnetic material of the motor. This loss acts like a resistor in parallel with the actuator coils and gives rise to an additional 15° of phase shift at 1 kHz. This negative phase shift in the loop transmission is distinct from the phase shift due to the inductance of the beam-steering coil, which was reduced to approximately 1° at crossover by means of a power amplifier with extremely high output impedance to frequencies in excess of 50 kHz. The design combines feedback to establish output current level with an open-loop common-base buffer amplifier to provide the high output impedance.

To achieve design objectives, the compensator included two integrators to increase low-frequency loop gain, two complex zeros located at 110 Hz with a damping ratio of 0.25, a zero at 400 Hz to introduce positive phase shift at crossover, and a second-order low-pass filter with a damping ratio of 0.707 located at 4 kHz. This low-pass filter reduced noise bandwidth and lowered loop gain at the frequency of the secondary resonance and, most important, added more than 90° of phase shift to make the resonance phase stable. In addition, a lead network furnishing about 20° of positive phase shift at 1 kHz was used to compensate the negative phase shift introduced by the lossy magnetic material. The loop transmission that results when this compensator is combined with the fixed-element dynamics shown earlier is also indicated in Figure 7. This figure was derived from the measured closed-loop rejection transfer function.

The uncompensated tracking error can be found from the closed-loop rejection transfer function. This function was measured using three different methods: (1) inject an error signal from inside the loop and measure the resulting tracking error internally; (2) inject a disturbance from outside the loop using the beam-steerer and measure the resulting tracking error internally; and (3) inject a disturbance from outside the loop using the beam-steerer and measure the resulting tracking error externally using the reference detector. For frequencies above 1 Hz, all three methods yielded the same results. However, below 1 Hz only the second method had sufficient resolution to obtain useful measurements below −120 dB. A possible reason that method (3) did not yield better low-frequency rejection measurements is because of 1/f noise in the reference detector. The results are shown in Figure 8. The closed-loop transfer function is also indicated in this figure. The angular disturbance of the beam-steerer at 0.1 Hz was approximately 1 mrad and, therefore, the 135 dB of rejection corresponds to a tracking error of less than 1 nrad.

The NEA as a function of signal power was measured by normalizing the rms voltage out of the reference detector by the angular gain of the detector with the disturbance generator turned off. The angular gain was accurately determined using two different methods. The first method involved a linear least-square fit to the measured central ±0.4 beamwidth of the angle discriminator. The second method involved inserting a precision optical wedge into the beam between the FSM and the first beamsplitter. The two methods agreed to within 5 percent. The average of the two measurements was used in subsequent analyses.

NEA was recorded for a variety of signal powers and APD gains. The results are plotted in Figure 9. Our NEA data were measured on an earlier design that featured a 500-Hz crossover frequency, and the vertical axis on the right corresponds to those measurements. The vertical axis on the left is the equivalent NESD. This was derived from the measured NEA using the measured noise bandwidth (2200 Hz). The noise bandwidth was found by numerical integration of the measured closed-loop

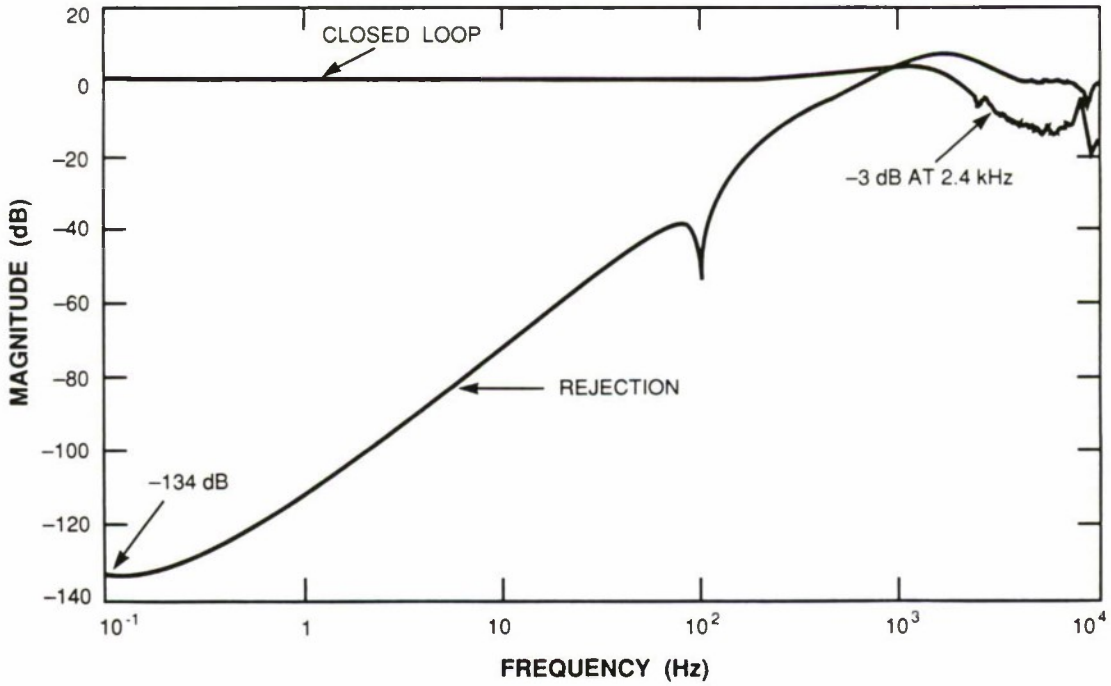

116455-8

Figure 8. Measured closed-loop transfer functions.

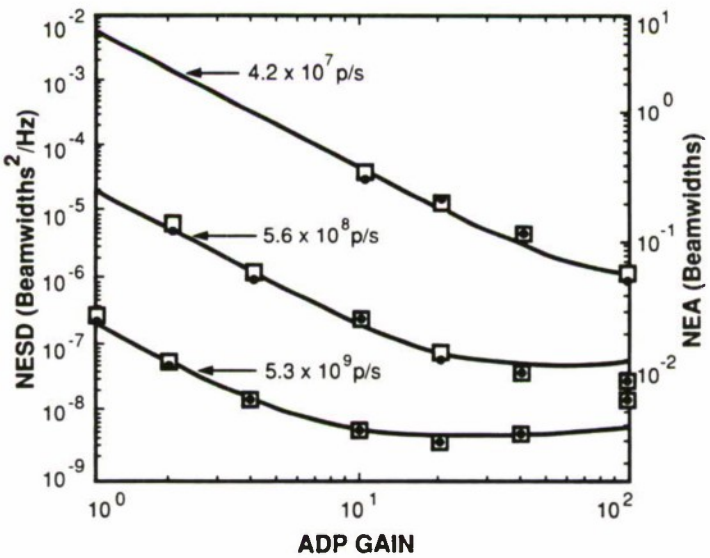

116455-9

Figure 9. NESD and NEA vs APD gain.

transfer function. The symbols represent the measured azimuth and elevation tracking errors, and the lines represent theoretical predictions based on the parameters in Table I. Sinusoidal intensity modulation with a modulation depth of 0.5 was used, and ~1.5 dB of implementation loss was assumed. Note that even with a noise-induced tracking error as low as 0.003 beamwidth, the equations developed earlier for NESD still accurately predict the performance.

It is of interest to compare the best tracking performance achieved at each of the three signal powers with the tracking performance bound of Equation (10). The best measured NESD values were 3.84×10^{-9}, 4.16×10^{-8}, and 1.59×10^{-6} BW^2/Hz for signal powers of 5.3×10^9, 5.6×10^8, and 4.2×10^7 p/s, respectively. The corresponding losses from the optimal value are easily calculated to be 10.0, 10.6, and 15.2 dB, respectively. Accounting for the suboptimal performance, we find 4.8 dB due to discriminator gain (Section 2.4.), 3 to 5 dB due to device noise (Section 2.5.), 1.5 dB due to implementation loss (above paragraph), and 1.0 dB in quantum efficiency (see Table I). Note that an additional loss of approximately 2.9 dB for the 4.2×10^7 p/s case is most likely accounted for by the fact that the optimum gain was above 100, as seen in Figure 8.

The system was designed to operate over a static and dynamic signal power range of 100 to 1. Various tests showed that the system performed quite well over this range. In addition to the static dynamic range capability displayed in Figure 9, we investigated the tracking performance in the presence of dynamic fades. We found that, in the presence of smooth or instantaneous fades, the NEA would simply increase from the high-signal-power value to the low-signal-power value. We also measured tracking system bias as a function of signal power, and found that the bias was limited to less than 0.05 beamwidth. The addition of a simple AGC circuit between the normalizing circuit and the sum-and-difference channels could be used to increase the dynamic range still further.

5. CONCLUSIONS

We have developed a variety of bounds for the noise-equivalent spectral density. Under signal shot-noise-limited operation, direct detection was shown to be able to outperform a heterodyne detection system by 3 dB. Also under signal shot-noise-limited operation, the performance of a quadrant detector was within 4.8 dB (2 dB) of being the optimal detector array for an Airy-disk (Gaussian) intensity distribution. As the background and device noise increase, the performance difference approaches zero. The optimal quadrant detector radius was approximately equal to the first null in the Airy-disk profile for background-limited operation. If the tracking detector array was optimized for centroid estimation, near-optimal tracking performance could still be achieved. Based on measured parameters, we showed that an APD-based tracking system can outperform a PIN-based tracking system by as much as 20 dB.

The effects of non-focal-plane processing and focus errors on tracking performance were quantified in terms of the effect on the NESD, system rejection, and dynamic range. We showed that to keep the loss in noise performance acceptably small, the focus error should be kept to less than $\lambda/13$ and that the detector array should be positioned to within the diffraction-limited spot size times the system f-number.

Our experimental results showed very good agreement with theoretical predictions. Over 2.4 kHz of closed-loop bandwidth, 134 dB of rejection at low frequencies, and tracking errors as low as $3/1000^{th}$ of a beamwidth were demonstrated. Low-noise performance was demonstrated using four single-element APDs and an image splitter.

REFERENCES

1. T.S. Wei and R.M. Gagliardi, "Direct Detection vs Heterodyning in Optical Beam Tracking," in *Phase Conjugation, Beam Combining, and Diagnostics*, R.A. Fisher and I. Abramowitz, Eds., Proc. SPIE **739**, 189-196 (1987).

2. K.J. Held and J.D. Barry, "Precision Optical Pointing and Tracking from Spacecraft with Vibrational Noise," in *Optical Technologies for Communication Satellites*, K. Bhasia, Ed., Proc. SPIE **616**, 160-173 (1986).

3. L.M. Germann, R. Nelson, and P.W. Young, "Pointing, Acquisition, and Tracking Subsystem for Space-Based Laser Communications," in *Optical Technologies for Communication Satellites*, K. Bhasia, Ed., Proc. SPIE **616**, 118-128 (1986).

4. L.G. Kazovsky, "Theory of Tracking Accuracy of Laser Systems," Opt. Eng. **22**, 339 (1983).

5. E.A. Swanson and V.W.S. Chan, "Heterodyne Spatial Tracking System for Optical Space Communication," IEEE Trans. Commun. **COM-34**, 118 (1986), DTIC AD-A172604.

6. J.H. McElroy *et al.*, "CO_2 Laser Communication Systems for Near-Earth Space Applications," IEEE Proc. **65**, 221 (1977).

7. R. Kern, U. Kugel, and E. Hettlage, "Control of a Pointing, Acquisition, and Tracking Subsystem for Intersatellite Laser Links ISL," in *Optical Systems for Space Applications*, H. Lutz and G. Otrio, Eds., Proc. SPIE **810**, 202-210 (1987).

8. R. Stanton *et al.*, "ASTROS: A sub-Arcsec CCD Star Tracker," in *State of the Art Imaging Arrays and Their Applications*, K. Prettyjohns, Ed., Proc. SPIE **501**, 256-282 (1984).

9. P.P. Webb, R.J. McIntyre, and J. Conradi, "Properties of Avalanche Photodiodes," RCA Rev. **35**, 234 (1974).

10. E.A. Swanson, E.R. Arnau, and F.G. Walther, "Measurements of Natural Radiation Effects in a Low-Noise Avalanche Photodiode," IEEE Trans. Nucl. Sci. **NS-34**, 1658 (1987).

11. H.L. Van Trees, *Detection, Estimation, and Modulation Theory — Part I* (Wiley, New York, 1968).

12. D.L. Snyder, *Random Point Processes* (Wiley, New York, 1975).

13. K. Winick, "Cramér-Rao Lower Bound on the Performance of Charge-Coupled-Device Optical Position Estimators," J. Opt. Soc. Am. A. **3**, 1809 (1986).

14. W.L. Wolfe and G.J. Zissis, *The Infrared Handbook* (Environmental Research Institute of Michigan, Office of Naval Research, Department of the Navy, 1978).

15. W.K. Pratt, *Laser Communication Systems* (Wiley, New York, 1969).

16. L.J. Sullivan, "Infrared Coherent Radar," in *CO_2 Laser Devices and Applications*, T.S. Hartwick, Ed., Proc. SPIE **227**, 148-161 (1980), DTIC AD-A102689.

REPORT DOCUMENTATION PAGE

1a. REPORT SECURITY CLASSIFICATION Unclassified	1b. RESTRICTIVE MARKINGS
2a. SECURITY CLASSIFICATION AUTHORITY	3. DISTRIBUTION/AVAILABILITY OF REPORT Approved for public release; distribution is unlimited.
2b. DECLASSIFICATION/DOWNGRADING SCHEDULE	
4. PERFORMING ORGANIZATION REPORT NUMBER(S) Technical Report 844	5. MONITORING ORGANIZATION REPORT NUMBER(S) ESD-TR-88-326
6a. NAME OF PERFORMING ORGANIZATION Lincoln Laboratory, MIT 6b. OFFICE SYMBOL *(If applicable)*	7a. NAME OF MONITORING ORGANIZATION Electronic Systems Division
6c. ADDRESS *(City, State, and Zip Code)* P.O. Box 73 Lexington, MA 02173-0073	7b. ADDRESS *(City, State, and Zip Code)* Hanscom AFB, MA 01731
8a. NAME OF FUNDING/SPONSORING ORGANIZATION HQ AF Systems Command 8b. OFFICE SYMBOL *(If applicable)* AFSC/XTKT	9. PROCUREMENT INSTRUMENT IDENTIFICATION NUMBER F19628-85-C-0002
8c. ADDRESS *(City, State, and Zip Code)* Andrews AFB Washington, DC 20334-5000	10. SOURCE OF FUNDING NUMBERS PROGRAM ELEMENT NO. 63789F; PROJECT NO. 270; TASK NO.; WORK UNIT ACCESSION NO.
11. TITLE *(Include Security Classification)* Design Considerations and Experimental Results for Direct-Detection Spatial Tracking Systems	
12. PERSONAL AUTHOR(S) Eric A. Swanson and James K. Roberge	
13a. TYPE OF REPORT Technical Report 13b. TIME COVERED FROM _____ TO _____	14. DATE OF REPORT *(Year, Month, Day)* 1989, April, 4 15. PAGE COUNT 28
16. SUPPLEMENTARY NOTATION None	
17. COSATI CODES FIELD / GROUP / SUB-GROUP	18. SUBJECT TERMS *(Continue on reverse if necessary and identify by block number)* optical communication intersatellite optical links precision tracking

19. ABSTRACT *(Continue on reverse if necessary and identify by block number)*

The effect of signal and background shot noise, as well as device noise, on the performance of a direct-detection spatial tracking system is investigated for arbitrary detector arrays assuming linear loop operation. The performance of quadrant detectors as a function of background radiation and detector radius is then analyzed and compared with some performance bounds. APD- and PIN-based tracking systems also are compared. The effects of non-focal-plane processing, focus error, and pupil walk on tracking performance are investigated. Experimental results of a 2.4-kHz two-axis tracking loop operating at low signal power using an APD quadrant detector are presented.

20. DISTRIBUTION/AVAILABILITY OF ABSTRACT ☐ UNCLASSIFIED/UNLIMITED ☒ SAME AS RPT. ☐ DTIC USERS	21. ABSTRACT SECURITY CLASSIFICATION Unclassified	
22a. NAME OF RESPONSIBLE INDIVIDUAL Lt. Col. Hugh L. Southall, USAF	22b. TELEPHONE *(Include Area Code)* (617) 981-2330	22c. OFFICE SYMBOL ESD/TML